



Discovery of an Enormous Ly α Nebula in a Massive Galaxy Overdensity at $z = 2.3$

Zheng Cai^{1,2,11}, Xiaohui Fan², Yujin Yang³, Fuyan Bian⁴, J. Xavier Prochaska¹, Ann Zabludoff², Ian McGreer², Zhen-Ya Zheng^{5,6}, Richard Green², Sebastiano Cantalupo⁷, Brenda Frye², Erika Hamden⁸, Linhua Jiang⁹, Nobunari Kashikawa¹⁰, and Ran Wang⁹

¹UCO/Lick Observatory, University of California, 1156 High Street, Santa Cruz, CA 95064, USA; zca@ucolick.org

²Steward Observatory, University of Arizona, 933 North Cherry Avenue, Tucson, AZ 85721, USA

³Korea Astronomy and Space Science Institute, 776 Daedeokdae-ro, Yuseong-gu Daejeon, Korea

⁴Research School of Astronomy & Astrophysics, Mount Stromlo Observatory, Cotter Road, Weston ACT 2611, Australia

⁵Instituto de Astrofísica, Pontificia Universidad Católica de Chile, 7820436 Santiago, Chile

⁶Chinese Academy of Sciences South America Center for Astronomy, 7591245 Santiago, Chile

⁷Institute for Astronomy, ETH Zurich, Wolfgang-Pauli-Strasse 27, 8093 Zurich, Switzerland

⁸California Institute Technology, 1200 East California Boulevard, Pasadena, CA, USA

⁹The Kavli Institute for Astronomy and Astrophysics, Peking University, Beijing 100871, P. R. China

¹⁰National Astronomical Observatory of Japan, Mitaka, Tokyo, 181-8588, Japan

Received 2016 September 13; revised 2017 January 20; accepted 2017 January 24; published 2017 March 3

Abstract

Enormous Ly α nebulae (ELANe), unique tracers of galaxy density peaks, are predicted to lie at the nodes and intersections of cosmic filamentary structures. Previous successful searches for ELANe have focused on wide-field narrowband surveys or have targeted known sources such as ultraluminous quasi-stellar objects (QSOs) or radio galaxies. Utilizing groups of coherently strong Ly α absorptions, we have developed a new method to identify high-redshift galaxy overdensities and have identified an extremely massive overdensity, BOSS1441, at $z = 2-3$. In its density peak, we discover an ELAN that is associated with a relatively faint continuum. To date, this object has the highest diffuse Ly α nebular luminosity of $L_{\text{nebula}} = 5.1 \pm 0.1 \times 10^{44} \text{ erg s}^{-1}$. Above the 2σ surface brightness limit of $\text{SB}_{\text{Ly}\alpha} = 4.8 \times 10^{-18} \text{ erg s}^{-1} \text{ cm}^{-2} \text{ arcsec}^{-2}$, this nebula has an end-to-end spatial extent of 442 kpc. This radio-quiet source also has extended C IV $\lambda 1549$ and He II $\lambda 1640$ emission on $\gtrsim 30$ kpc scales. Note that the Ly α , He II, and C IV emissions all have double-peaked line profiles. Each velocity component has an FWHM of $\approx 700-1000 \text{ km s}^{-1}$. We argue that this Ly α nebula could be powered by shocks due to an active galactic nucleus-driven outflow or photoionization by a strongly obscured source.

Key words: galaxies: high-redshift – intergalactic medium

1. Introduction

During the peak epoch of galaxy formation at $z = 2-3$ (e.g., Bouwens et al. 2011), most of the baryons in the universe reside outside galaxies; they lie within the intergalactic medium (IGM) and circumgalactic medium (CGM; e.g., Cen et al. 1994; Hernquist et al. 1996; Miralda-Escudé et al. 1996; Rauch 1998). The IGM and CGM provide a vast reservoir for fueling the star formation of galaxies and also serve as a “sink” for metals driven from the galactic feedback (e.g., Prochaska et al. 2011; Tumlinson et al. 2011). On the other hand, the properties and structures of the IGM/CGM, such as kinematics, morphology, and metallicity, are increasingly reshaped by the energetic processes occurring in galaxies, and therefore the IGM/CGM acts as a laboratory to stringently constrain the physics of the galaxy formation (e.g., Fumagalli et al. 2011).

Intergalactic/circumgalactic filaments have been studied via quasi-stellar object (QSO) absorption lines (e.g., Rauch 1998). But QSO absorption studies are limited by the sparseness of background QSOs. To reveal the connection of intergalactic gas to galaxies and their CGM (i.e., on scales of ~ 100 kpc), one must constrain the full three-dimensional intergalactic/circumgalactic material using more numerous, but fainter, background galaxy populations (e.g., Lee et al. 2014) or directly map the faint diffuse emission of the IGM or CGM (e.g., Cantalupo et al. 2014; Martin et al. 2015; Borisova et al. 2016). The Ly α line is the primary coolant of gas with

$T \sim 10^4 \text{ K}$ and can be used to trace the CGM/IGM via emission. Such Ly α nebulae provide to us an indispensable opportunity to study the CGM in emission.

Theoretical models suggest that several mechanisms may generate circumgalactic Ly α emission: (1) recombination radiation following photoionization (fluorescence) powered by ultraviolet (UV) sources (Gould & Weinberg 1996; Cantalupo et al. 2005; Geach et al. 2009; Kollmeier et al. 2010), (2) cooling radiation due to the gravitationally heated gas (Fardal et al. 2001; Yang et al. 2006; Dijkstra & Loeb 2009; Faucher-Giguère et al. 2010), (3) radiation from shock-heated gas driven by the feedback of galactic outflow (e.g., Taniguchi & Shioya 2000; Wilman et al. 2005; Villar-Martín et al. 2007), and (4) resonant scattering of Ly α from the embedded source (Dijkstra & Loeb 2009; Hayes et al. 2011; Cantalupo et al. 2014; Geach et al. 2014, 2016). The photoionization radiation is generated when the dense regions of the CGM are photoionized by strong ionizing sources and then recombine to emit Ly α photons. The cooling radiation is the Ly α photons released when gas settles into galactic potential wells (e.g., Yang et al. 2006). Shock-heating can be powered by supernovae or by relativistic winds or jets resulting from gas accretion onto supermassive black holes (SMBHs). Ly α resonant scattering produces extended Ly α halos as Ly α photons propagate outward and is characterized by a double-peaked structure of the resonant emission lines (e.g., Yang et al. 2014). These mechanisms are believed to power the extended Ly α emission in high-density regions of the early universe. The Ly α nebulae/blobs (LABs) are expected to occupy massive

¹¹ Hubble Fellow.

dark matter halos ($\sim 10^{13} M_{\odot}$), representing sites of the most active star formation and tracing large-scale mass overdensities (e.g., Steidel et al. 2000; Prescott et al. 2009; Yang et al. 2009).

A few observational efforts have been made to search for Ly α nebulae/blobs at $z = 2-3$. These successful searches include narrowband imaging surveys of random fields (e.g., Steidel et al. 2000; Francis et al. 2001; Palunas et al. 2004; Dey et al. 2005; Prescott et al. 2009; Yang et al. 2009, 2010), narrowband imaging of known overdensities (Matsuda et al. 2005), and targeting of biased halo tracers, such as ultraluminous QSOs (e.g., Cantalupo et al. 2014; Hennawi et al. 2015) and radio galaxies (e.g., Heckman et al. 1991; Villar-Martín et al. 2007; Miley & De Breuck 2008). Using VLT/MUSE, Borisova et al. (2016) present a blind survey for Ly α nebulae associated with the 17 brightest radio-quiet QSOs at $3 < z < 4$. They find that 100% of the QSOs are associated with Ly α nebulae with linear sizes of $\sim 100-320$ kpc. In this sample, the relatively narrow Ly α FWHMs ($300-600 \text{ km s}^{-1}$) are consistent with a fluorescent powering mechanism. Increasing evidence has shown that the Ly α nebulae often lie in regions that contain both enhanced UV radiation (or nearby UV sources) and gas overdensities (Hennawi & Prochaska 2013; Hennawi et al. 2015).

The extended He II and C IV emissions associated with Ly α nebulae contain crucial information about the powering mechanisms. The extended C IV line allows us to estimate the metallicity of the CGM gas and the size of the metal-enriched halos (Arrigoni Battaia et al. 2015b). In turn, such metal-line emission allows us to examine whether the shocks of the galactic outflow could power the LABs (e.g., Villar-Martín et al. 1999, 2007; Allen et al. 2008; Arrigoni Battaia et al. 2015a). Arrigoni Battaia et al. (2015b) conducted a deep survey of 13 Ly α blobs in the SSA22 overdensity (Steidel et al. 2000; Matsuda et al. 2005), targeting the He II $\lambda 1640$ and C IV $\lambda 1549$. These observations did not detect extended He II and C IV emission in any of the LABs, suggesting that photoionization could be a major powering mechanism. Borisova et al. (2016) also did not detect strongly extended He II and C IV emission in their sample of 17 ultraluminous QSOs, indicating a large fraction of the gas in massive QSO host halos at $z = 3-4$ could be cold ($T \sim 10^4$ K) and metal-poor ($Z < 0.1 Z_{\odot}$). Prescott et al. (2009) detect a LAB that has a spatial extent of 80 kpc at $z \approx 1.67$ associated with extended C IV and He II. The Ly α , C IV, He II, and C III] lines all show a coherent velocity gradient of 500 km s^{-1} , strongly indicating a 50-kpc-large rotational disk illuminated by an AGN.

Recently, two enormous Ly α nebulae (ELANe) have been discovered to have a large spatial extent of $\gtrsim 400$ kpc (Cantalupo et al. 2014; Hennawi et al. 2015). These ELANe further offer excellent laboratories to detect and map the gas in the dense part of the IGM, and to study how the IGM feeds star formation in massive halos (Martin et al. 2014, 2015). Arrigoni Battaia et al. (2015b) conducted deep spectroscopic integrations targeting He II and C IV emission and report a null detection, suggesting ELANe are mainly due to AGN photoionization on the cool, metal-poor CGM gas.

In this paper, we report a discovery of another ultraluminous ELAN that resides near the density peak of our newly discovered massive overdensity BOSS1441 at $z = 2.32 \pm 0.02$ (Cai et al. 2016). This nebula has a projected linear size of ≈ 450 kpc, comparable with the Slug nebula (Cantalupo et al. 2014), and remarkably extended He II and C IV emission over

$\gtrsim 30$ kpc. The Ly α , He II, and C IV lines all show double-peaked kinematics, with each component having line widths of $700-1000 \text{ km s}^{-1}$. The large spatial extent of Ly α emission, the strongly extended He II and C IV, and the emission-line structures and kinematics all make this ELAN unique. This Ly α nebula resides in an overdense field selected by utilizing the largest QSO spectral library from the Baryon Oscillations Spectroscopic Survey (BOSS; e.g., Dawson et al. 2013). It contains a group of extremely rare, high optical depth Ly α absorption (Cai et al. 2015a) arising from the IGM overdensity and a rare QSO group (e.g., Cai et al. 2016). We refer to this program as MAPPING the Most Massive Overdensity Through Hydrogen (MAMMOTH) (Cai et al. 2015a). In this paper, we refer to this nebula as MAMMOTH-1.

This paper is structured as follows. In Section 2, we introduce the selection of MAMMOTH-1 and our follow-up observations. In Section 3, we discuss our observational results. In Section 4, we discuss the physical properties and several powering mechanisms that could be responsible for such a unique ELAN. We also estimate the cool gas mass. We give a brief summary in Section 5. We convert redshifts to physical distances assuming a Λ CDM cosmology with $\Omega_m = 0.3$, $\Omega_{\Lambda} = 0.7$, and $h = 0.70$ (h_{70}). Throughout this paper when measuring distances, we normally refer to physical separations or distances. We use cMpc to represent comoving megaparsecs, and kpc to represent physical kiloparsecs.

2. Observations

2.1. Target Selection

MAMMOTH-1 is located in the density peak of the large-scale structure BOSS1441 (Cai et al. 2016). BOSS1441 was selected because this field contains a group of five strong Ly α absorption systems within a $20 h^{-1}$ comoving Mpc (cMpc) scale at $z = 2.32 \pm 0.03$. Each Ly α absorption has an effective optical depth on a scale of $15 h^{-1}$ cMpc of $\tau_{\text{eff}}^{15h^{-1} \text{ Mpc}} > 3 \times$ the mean optical depth ($\langle \tau_{\text{eff}} \rangle$). These absorption systems are not due to damped Ly α absorption (DLA). Two of them have $\tau_{\text{eff}}^{15h^{-1} \text{ Mpc}} > 4.5 \times \langle \tau_{\text{eff}} \rangle$, and the optical depth is higher than the threshold of coherently strong Ly α absorption (CoSLA; see Cai et al. 2016). This group of absorbers satisfies the selection criteria (a)–(d2) proposed in Cai et al. (2015a). The redshift is chosen by our custom narrowband filter NB403.

The NB403 filter has a central wavelength of $\lambda_c = 4030 \text{ \AA}$ and a bandwidth of FWHM = 45 \AA . The NB filter is very efficient in searching for the overdensities because (1) the BOSS QSO density peak lies at $z \sim 2.3$. With a NB filter at a similar redshift, we can fully take advantage of the SDSS Ly α forest survey; (2) the KPNO-4 m/MOSAIC camera is highly sensitive at $\sim 4000 \text{ \AA}$. In addition, $z \sim 2.3$ is a good redshift for studying galaxy properties using ground-based telescopes. Optical and infrared spectrographs can fully cover the emission lines from Ly α to H α .

2.2. KPNO-4 m/MOSAIC Narrowband and Broadband Imaging

After selecting the BOSS1441 field, we conducted deep narrowband and broadband imaging and multiobject spectroscopy to select and confirm Ly α -emitting galaxies (LAEs). We used the KPNO-4 m/MOSAIC-1.1 camera for deep imaging with a custom narrowband filter NB403 and the Bw broadband

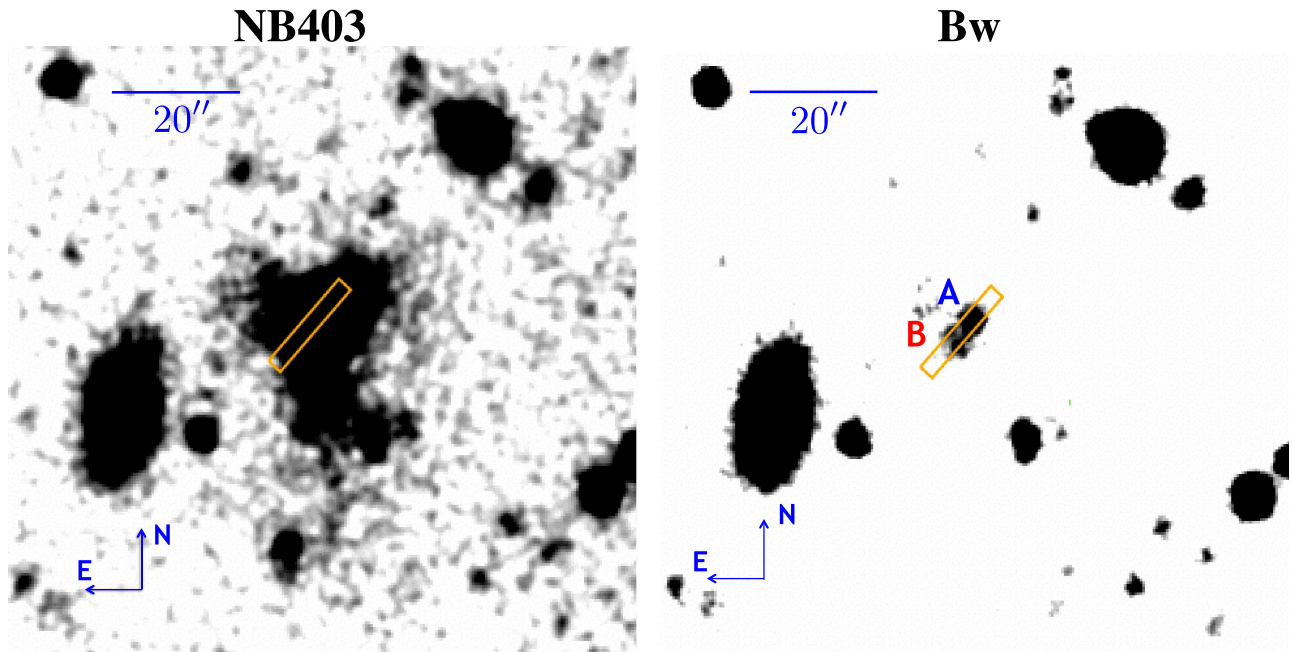


Figure 1. Final stacked images of the field surrounding MAMMOTH-1 overlotted with our LBT/MODS slit (orange rectangle). Each image has an area of $80''$ centered on the $\text{Ly}\alpha$ nebula. The narrowband (NB403) image at the $\text{Ly}\alpha$ line of the redshift of MAMMOTH-1 ($z = 2.32$) is in the left panel. The deep Bw-band image (middle panel) does not show any extended emission associated with MAMMOTH-1. We put the spectral slit (orange slit) containing the brightest two sources (A, B) in the center of MAMMOTH-1.

filter. These deep imaging observations were designed to reveal LAEs in the BOSS1441 field.

We briefly review our observations in the BOSS1441 field. More details can be found in Cai et al. (2016). The BOSS1441 field was observed on 2013 March, 2014 April, and 2014 June. For the NB403 filter, the total exposure time was 17.9 hr, which consisted of individual 15 or 20 minute exposures with a standard dither pattern to fill in the gaps between the eight MOSAIC CCD chips. The seeing ranged from $1''.1$ to $1''.7$, with the median seeing about $1''.32$. For the Bw filter, the total exposure time is 3 hr, which consists of individual 8-minute exposures with a fill gap dither pattern. The seeing for taking the Bw band ranges from $1''.1$ to $1''.8$, with the median value of $1''.37$. Around the LAE density peak region, we discovered a strong, highly extended $\text{Ly}\alpha$ emission: the ELAN MAMMOTH-1, which is detected in each individual frame with a 15–20 minute exposure. The broadband filter (Bw) was observed for a total of 3 hr to match the depth of the narrowband filter. These observing conditions enable us to achieve a narrowband magnitude of $m_{\text{NB403}} = 25.1$ at 5σ (aperture: $2''.5$) and Bw-band magnitude $m_{\text{Bw}} = 25.9$ at 5σ . This depth corresponds to a 1σ $\text{Ly}\alpha$ surface brightness limit of $\text{SB}_{\text{Ly}\alpha} = 2.4 \times 10^{-18} \text{ erg s}^{-1} \text{ cm}^{-2} \text{ arcsec}^{-2}$.

2.3. LBT Imaging and Multiobject Spectroscopy

We used the Large Binocular Camera (LBC) on the Large Binocular Telescope (LBT) to obtain deep imaging using the U , V , and i broadband filters. The LBC imaging enables the selection of the star-forming galaxies at $z \approx 2.3$ (e.g., Adelberger et al. 2005) and helps to eliminate [O II] contaminants using the BX galaxy selection technique.

We also used the Dual channel of the Medium-Dispersion Grating Spectroscopy (MODS) (Byard & O’Brien 2000) on the LBT to spectroscopically confirm the redshifts of galaxies and the $\text{Ly}\alpha$ nebula in the BOSS1441 overdense field. The LBT/MODS

provides high efficiency over $3200\text{--}10,000 \text{ \AA}$ with a resolution of $R = 2000$. We used a dichroic that divides the incoming beam at $\approx 5700 \text{ \AA}$. This configuration covers $\text{Ly}\alpha$ and a few interstellar lines, for example, C IV $\lambda 1550$, He II $\lambda 1640$, and C III] $\lambda 1907/1909$, for galaxies at $z = 2.3$.

We used a MODS mask to observe the MAMMOTH-1 nebula and other LAEs in the field. The total exposure time was 6 hr. Each mask was split into six 1800 s integrations, with a typical seeing of $1''$. The slit length on the MAMMOTH-1 nebula is $10''$ (Figure 1).

The MODS data reduction followed the LBT/MODS reduction routine. First, each raw image was processed with the MODS CCD reduction utilities (modsTools v03) to obtain bias-subtracted and flat-fielded images. We generated polynomial fits to the arc calibration to determine the transformation between image pixels and wavelength. The sky model was fit to each image using B-splines and then subtracted. We used LACOSMIC (van Dokkum 2001) to identify cosmic rays during the construction of the sky model. The individual exposures were combined with inverse variance weighting to produce the final 2D spectrum.

3. Observational Results

3.1. Mapping the $\text{Ly}\alpha$ Emission

In Figure 1, we present the stacked images of MAMMOTH-1 in both the NB403 narrowband and Bw broadband images. We also overplot the LBT/MODS spectral slit. From this figure, we detect extended structures in both the narrowband (NB403, left panel) and broadband images (Bw, right panel). In the Bw broadband, we detect multiple sources associated with MAMMOTH-1. In Figure 2, we present the continuum-subtracted $\text{Ly}\alpha$ image. We smooth the image using a Gaussian kernel with $1''$ (Cantalupo et al. 2014; Hennawi et al. 2015). Within the 2σ ($4.8 \times 10^{-18} \text{ erg s}^{-1} \text{ cm}^{-2} \text{ arcsec}^{-2}$) surface

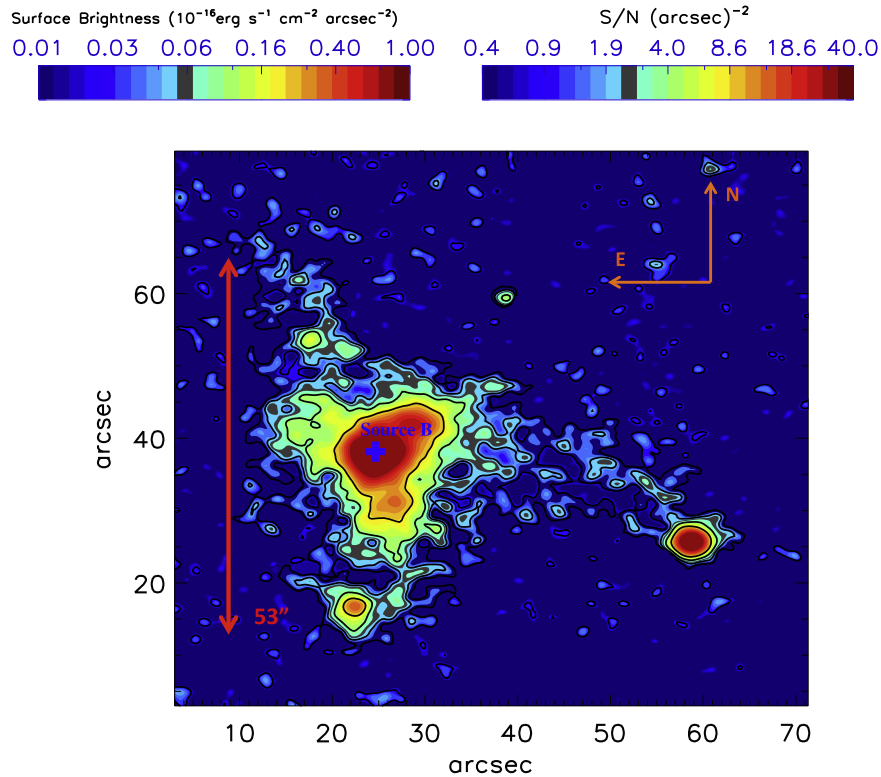


Figure 2. Continuum-subtracted, smoothed narrowband image of the field around the enormous Ly α nebula (ELAN) MAMMOTH-1. The color map and contours indicate the Ly α surface brightness (left color bar) and the signal-to-noise ratio per arcsec² aperture (right color bar), respectively. This image reveals the Ly α emission of the enormous Ly α nebula (ELAN). The current 1σ surface brightness limit is $2.4 \times 10^{-18} \text{ erg s}^{-1} \text{ cm}^{-2} \text{ arcsec}^{-2}$. Above the flux contour of SB $> 4.8 \times 10^{-18} \text{ erg s}^{-1} \text{ cm}^{-2} \text{ arcsec}^{-2}$, MAMMOTH-1 has a total luminosity of $L = 5.28 \pm 0.07 \times 10^{44} \text{ erg s}^{-1}$. Further, we tentatively detect filamentary structures around MAMMOTH-1.

brightness contour, this ELAN has an end-to-end projected extent of 53 arcsec (442 physical kpc).

In the broadband image, the brightest two sources, brighter source A ($B_{AB} \approx 23.5$, $i_{AB} \approx 22.5$) and fainter source B ($B_{AB} \approx 25.1$, $i_{AB} \approx 24.3$), are marked in Figure 1. Source B resides in the flux peak of the broadband-subtracted narrowband image. Our LBT/MODS spectroscopy shows that source A is a low-redshift AGN at $z = 0.16$, while source B is an object at $z = 2.32$. In Figure 3, we present the 1D spectrum of source B, which has strong emission in Ly α , He II, C IV, and C III]. Using LBT/LBC imaging, we find that source B has a brightness of $U_{AB} = 25.77 \pm 0.07$, $V_{AB} = 24.37 \pm 0.03$, and $i_{AB} = 24.30 \pm 0.03$. Although it is difficult to identify all of the possible powering sources associated with MAMMOTH-1, source B’s location and redshift suggest that it could be the dominant powering source of MAMMOTH-1. We use source B’s position as the center of MAMMOTH-1: $\alpha = 14:41:27.62$, $\delta = +40:03:31.44$.

From the broadband-subtracted narrowband image (Figure 2), we measure that MAMMOTH-1 has a total Ly α luminosity of $5.28 \pm 0.07 \times 10^{44} \text{ erg s}^{-1}$. Unlike ELANs powered by ultra-luminous type-I QSOs, the Ly α emission of MAMMOTH-1 arises mainly from the diffuse nebula rather than from the point-spread function (PSF). In Figure 4, we present the radial profile of MAMMOTH-1’s surface brightness. This ELAN has an extremely high extended nebular luminosity, and the central PSF contributes only 4% of the total Ly α luminosity. If we subtract the Ly α PSF (source B in Figure 1), MAMMOTH-1 has an extended nebular Ly α luminosity of $5.07 \pm 0.07 \times 10^{44} \text{ erg s}^{-1}$, the highest

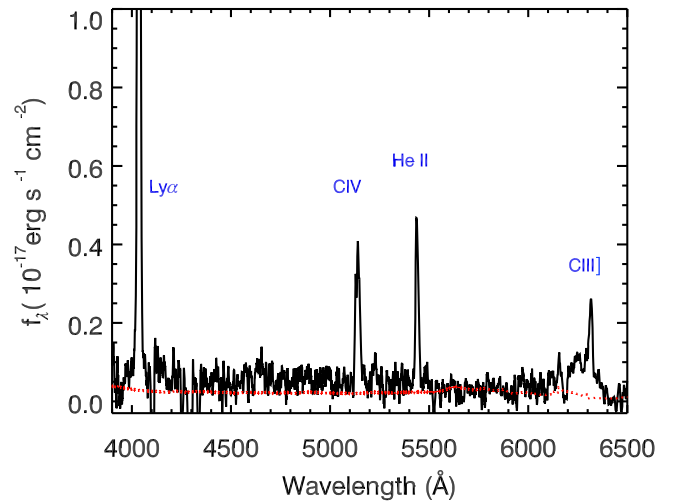


Figure 3. LBT/MODS spectrum of the enormous Ly α nebula (ELAN) MAMMOTH-1 at $z = 2.32$ centered on source B in Figure 1. This spectrum is taken using a long slit with a $2''$ slit width. The red dotted line represents the error of the spectrum.

discovered to date. We summarize the size and luminosity of MAMMOTH-1 in Table 1.

In Figure 2, the northern/eastern part of MAMMOTH-1 seems to have a filamentary structure. If this filamentary structure is real, it aligns in the same direction as the morphology of the large-scale structures (see Cai et al. 2016). In the cosmic hierarchical nature of structure formation, large-scale filaments are formed from the merging of small-scale

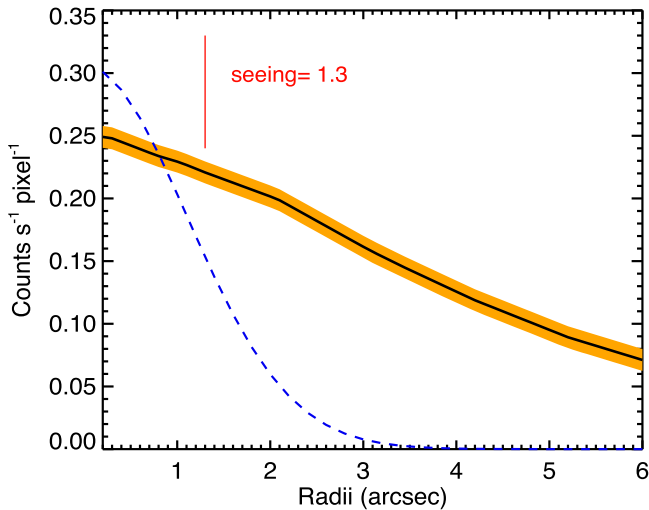


Figure 4. Surface brightness as a function of radii. MAMMOTH-1 has a very extended profile (black line). The orange area represents the 1σ error of the radial profile. We use source B’s position (Figure 1) as the center of MAMMOTH-1. The blue dashed line represents the central point-spread function (PSF). The PSF is constructed using an FWHM that is equal to the seeing of $1''.3$. The amplitude is determined assuming that all of the ELAN’s luminosity within the Moffat FWHM is contributed by the PSF. The central PSF constitutes only 4% of entire flux of MAMMOTH-1.

Table 1
Properties of Ly α Nebula MAMMOTH-1

Center ^a	Aperture	L_{total} (10^{43} erg s $^{-1}$)	L_{nebula} (10^{43} erg s $^{-1}$)
$\alpha = 14:41:27.62,$ $\delta = +40:03:31.44$	Entire nebula ^b	52.8 ± 2.0	49.0 ± 1.0

Notes.

^a We apply source B’s position as the center of MAMMOTH-1 (see Figures 1 and 2).

^b We include all of the continuous area with surface brightness (SB) $> 4.8 \times 10^{-18}$ erg s $^{-1}$ cm $^{-2}$ arcsec $^{-2}$.

pieces. Simulations suggest that cosmic webs containing baryonic matter tend to align with underlying large-scale structures of dark matter (e.g., Cen et al. 1994; Fukugita & Peebles 2004; Colberg et al. 2005; Cen & Ostriker 2006; Hellwing 2014). Our observations tentatively support these simulations.

3.2. Emission-line Profiles

The deep LBT/MODS spectra reveal Ly α , He II, C IV, and C III] emission (Figure 4). Both C IV and He II extend over $\gtrsim 30$ kpc scales (Figure 5). Extended He II and C IV emissions have been observed previously in radio galaxies, but MAMMOTH-1 is unlikely to be powered by a radio jet. From the FIRST radio catalog (Becker et al. 1995), we do not find any radio-loud sources with a radio flux at 1.4 GHz $F(1.4 \text{ GHz}) > 0.9$ mJy in the area within 30 arcsec of the MAMMOTH-1 nebula. We use the redshift of the nonresonant He II $\lambda 1640$ line as the redshift of MAMMOTH-1, yielding $z = 2.319 \pm 0.004$.

The Ly α , C IV, and He II line profiles reveal two main components. In Figure 5, we fit these lines with two Gaussians. For the Ly α line, the blue component has a best-fit FWHM of 876 ± 120 km s $^{-1}$, and the red component has a best-fit

FWHM of 1140 ± 160 km s $^{-1}$. The redshift offset between the two components is ≈ 700 km s $^{-1}$. For the He II line, the blue component has an FWHM of 714 ± 100 km s $^{-1}$, and the red component has a best-fit FWHM of 909 ± 130 km s $^{-1}$. The offset between the two components is the same as that of Ly α .

3.3. Flux and Surface Brightness

In our LBT/MODS spectra, the slit is $10''$ long and $2''$ wide. We measure the flux of Ly α , He II, C IV, and C III]. The aperture we applied is 15 ± 5 kpc ($1.8 \pm 0''.6$) away from source B along the slit direction and within 3000 km s $^{-1}$ in the wavelength direction (see blue rectangle in Figure 5), sufficiently large to include all of the diffuse emission in the wavelength direction. This gives a size of $2''$ (slit width) \times $1''.2$ (along the slit direction). We apply this aperture to measure the surface brightness of the emission lines. We regard the flux as the CGM emission at $R = 1''.8$ (15 kpc) away from the central source.

Applying this aperture to the LBT/MODS 2D spectrum (Figure 5), we determine that the Ly α emission (first panel) has a flux of $f_{\text{Ly}\alpha, 15 \text{ kpc}} = 6.6 \pm 0.2 \times 10^{-16}$ erg s $^{-1}$ cm $^{-2}$, corresponding to $L_{\text{Ly}\alpha, 15 \text{ kpc}} = 1.7 \times 10^{43}$ erg s $^{-1}$. The surface brightness of Ly α is $\text{SB}_{\text{Ly}\alpha, 15 \text{ kpc}} = 2.99 \pm 0.01 \times 10^{-16}$ erg s $^{-1}$ cm $^{-2}$ arcsec $^{-2}$.

The extended He II emission (second panel of Figure 5) has a line flux of $f_{\text{He II}, 15 \text{ kpc}} = 7.8 \pm 0.2 \times 10^{-17}$ erg s $^{-1}$ cm $^{-2}$, corresponding to a luminosity of $L_{\text{He II}, 15 \text{ kpc}} = 3.2 \pm 0.1 \times 10^{42}$ erg s $^{-1}$, and a surface brightness $\text{SB}_{\text{He II}, 15 \text{ kpc}} = 3.3 \pm 0.1 \times 10^{-17}$ erg s $^{-1}$ cm $^{-2}$ arcsec $^{-2}$.

The extended C IV emission (third panel of Figure 5) has a line flux of $f_{\text{C IV}, 15 \text{ kpc}} = 8.8 \pm 0.2 \times 10^{-17}$ erg s $^{-1}$ cm $^{-2}$, corresponding to $L_{\text{C IV}, 15 \text{ kpc}} = 3.6 \pm 0.1 \times 10^{42}$ erg s $^{-1}$ and $\text{SB}_{\text{C IV}, 15 \text{ kpc}} = 3.7 \pm 0.1 \times 10^{-17}$ erg s $^{-1}$ cm $^{-2}$ arcsec $^{-2}$.

The C III] emission (fourth panel of Figure 5) has a line flux of $f_{\text{C III}], 15 \text{ kpc}} = 0.9 \pm 0.2 \times 10^{-17}$ erg s $^{-1}$ cm $^{-2}$, corresponding to $L_{\text{C III}], 15 \text{ kpc}} = 0.4 \pm 0.1 \times 10^{42}$ erg s $^{-1}$ and $\text{SB}_{\text{C III}], 15 \text{ kpc}} = 0.4 \pm 0.1 \times 10^{-17}$ erg s $^{-1}$ cm $^{-2}$ arcsec $^{-2}$. We summarize our surface brightness measurements in Table 2.

3.4. Comparison between MAMMOTH-1 and Other Ly α Nebulae

In Figure 6, we present the sizes and Ly α luminosities for different Ly α nebulae from the literature in comparison with MAMMOTH-1. The Ly α emission from the central source has also been included. The typical size measurements for these objects are above surface brightness contours of $\sim 5 \times 10^{-18}$ erg s $^{-1}$ cm $^{-2}$ arcsec $^{-2}$, comparable to our measurements for MAMMOTH-1, which are above 4.8×10^{-18} erg s $^{-1}$ cm $^{-2}$ arcsec $^{-2}$. If we restrict the size measurements to the surface brightness contour of 4.8×10^{-18} erg s $^{-1}$ cm $^{-2}$ arcsec $^{-2}$, MAMMOTH-1 has a size similar to the Slug nebula (Cantalupo et al. 2014). But note that Cantalupo et al. (2014) reached a factor of $3 \times$ deeper than our current narrowband imaging, so the MAMMOTH-1 nebula may be extended on an even larger scale in deeper data. In Table 3, we further compare the diffuse nebular luminosities (excluding the PSF contribution). MAMMOTH-1 has the highest diffuse nebular luminosity among all of the confirmed Ly α nebulae and ELANe.

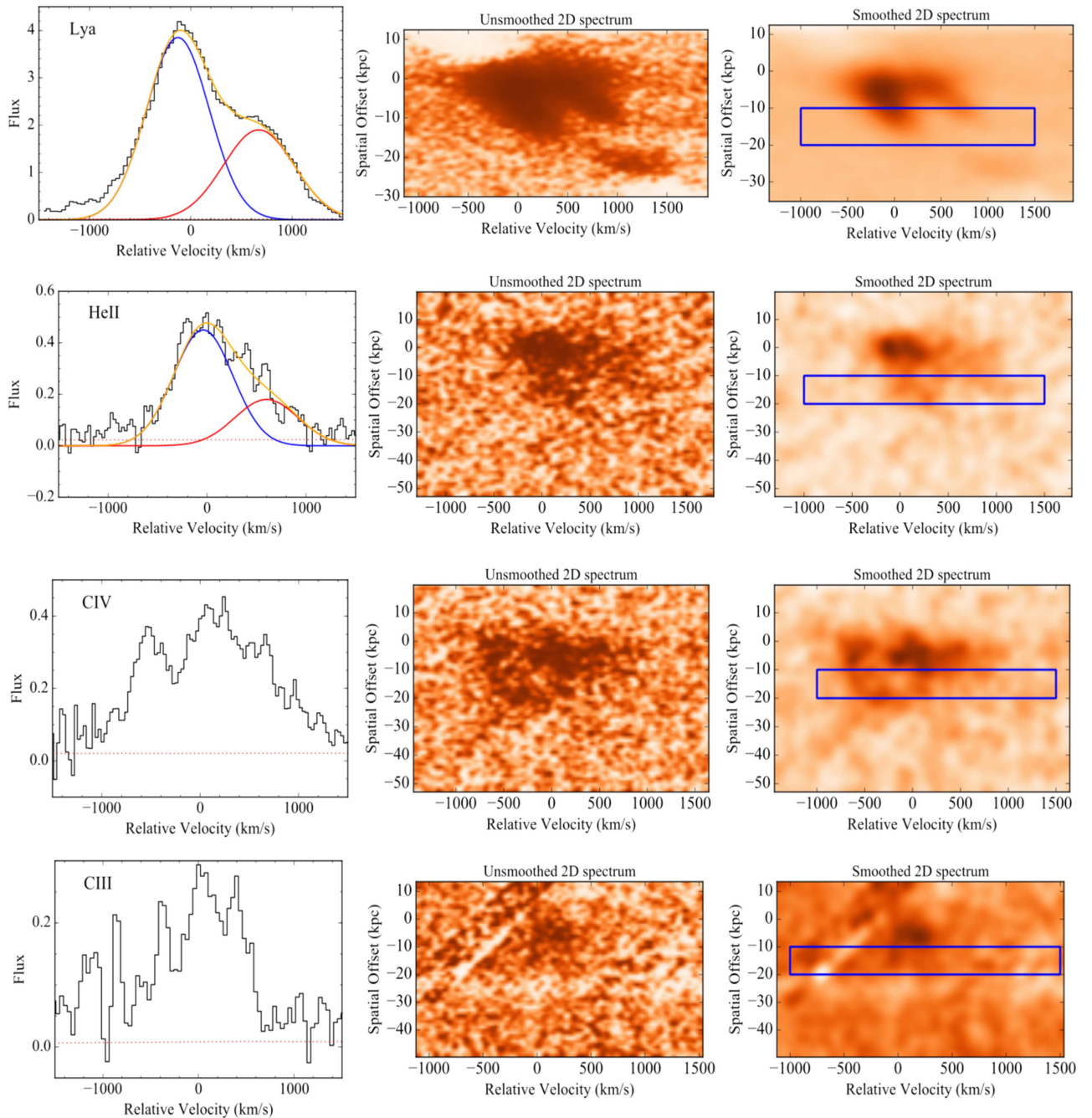


Figure 5. Spectra of emission lines of MAMMOTH-1 observed in LBT/MODS. From top to bottom: Ly α , He II, C IV, and C III]. Left column: 1D zoom-in of line profiles of Ly α , He II, C IV, and C III] (from top to bottom) as a function of the rest-frame velocity centered on the redshift of the nebula, measured from the He II line. We use two Gaussian functions to fit the two major components of Ly α and He II. Our spectral resolution is $R \approx 1000$ for this slit ($2''$ wide), corresponding to 91 km s^{-1} in the rest frame of MAMMOTH-1. The measured FWHM for each component is much wider than the spectral resolution. The deviation of C III] emission in the left wing is due to imperfect sky subtraction. Middle column: the unsmoothed 2D spectra of Ly α , He II, C IV, and C III]. Right column: the 2×2 pixel smoothed spectra of Ly α , He II, C IV, and C III]. From the spectrum, the extended Ly α emission lies in the spatial direction along the slit ($10''$). The C IV extends 33 physical kpc, and He II extends 31 physical kpc. The C III] is on a much smaller scale than C IV and He II. We show the aperture for measuring the surface brightness (blue rectangles).

4. Discussion

In the previous section, we showed that the ELAN MAMMOTH-1 has a Ly α spatial extent of ≈ 440 kpc and a total luminosity of $5.28 \pm 0.07 \times 10^{44} \text{ erg s}^{-1}$. This nebula resides in an extremely overdense galaxy environment previously discovered at $z = 2.3$. Moreover, this radio-quiet nebula has strongly extended He II, C IV, and C III] emission

(Figure 4). The Ly α , He II, and C IV line profiles are all double-peaked. In Table 3, we compare the properties of MAMMOTH-1 to other ELANe recently discovered. The Ly α spatial extent and the strong emission of C IV and He II make MAMMOTH-1 unique. In this section, we derive the physical properties of MAMMOTH-1, and we discuss several possible physical explanations for powering this ELAN.

Table 2
Surface Brightness of Emission Lines in MAMMOTH-1 Nebula (Blue Apertures in Figure 5)

Aperture	SB_{total} ($\text{erg s}^{-1} \text{cm}^{-2} \text{arcsec}^{-2}$)	SB_{CIV} ($\text{erg s}^{-1} \text{cm}^{-2} \text{arcsec}^{-2}$)	SB_{HeII} ($\text{erg s}^{-1} \text{cm}^{-2} \text{arcsec}^{-2}$)	SB_{CIII} ($\text{erg s}^{-1} \text{cm}^{-2} \text{arcsec}^{-2}$)
$2'' \times 1''.2$ ($16.7 \times 10 \text{ kpc}^2$)	$29.9 \pm 0.1 \times 10^{-17}$	$3.7 \pm 0.1 \times 10^{-17}$	$3.3 \pm 0.1 \times 10^{-17}$	$1.0 \pm 0.1 \times 10^{-17}$

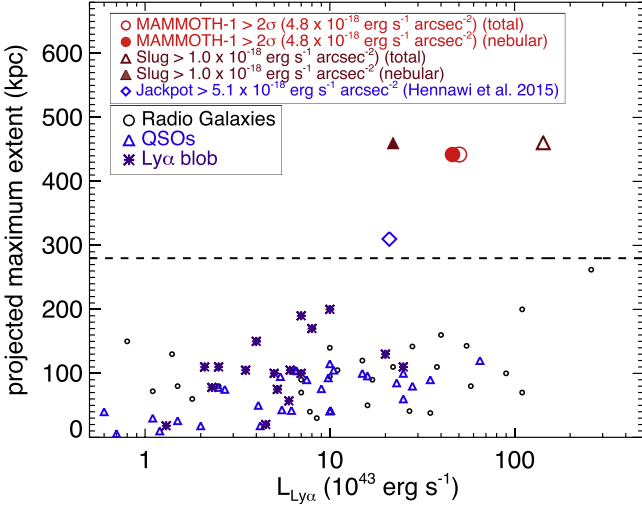


Figure 6. Projected maximum extent vs. total Ly α luminosity for different objects from the literature. The typical size measurement is above a surface brightness contour of $5 \times 10^{-18} \text{ erg s}^{-1} \text{ cm}^{-2} \text{ arcsec}^{-2}$. If we restrict the size measurement to contours above $4.8 \times 10^{-18} \text{ erg s}^{-1} \text{ cm}^{-2} \text{ arcsec}^{-2}$, our target MAMMOTH-1 is one of the most extended sources, with a spatial extent comparable to the Slug nebula. The open circle represents the total Ly α luminosity of MAMMOTH-1, and the solid circle represents the nebular luminosity, excluding the contribution from the central point-spread function (PSF). The luminosities of Slug nebula are cited from Cantalupo et al. (2014). The black dashed line shows the virial diameter of a dark matter halo of mass $M \sim 10^{12.5} M_{\odot}$, the typical host of radio-quiet QSOs (Martin et al. 2012, Cantalupo et al. 2014).

4.1. Ionizing Radiation

A comparison between hydrogen-ionizing photons and helium-ionizing photons constrains the hardness of the ionizing radiation. The number of H⁺-ionizing photons can be expressed as

$$Q(\text{H}) = \frac{L_{\text{Ly}\alpha, 15 \text{ kpc}}}{h\nu_{\text{Ly}\alpha}} \frac{1}{0.68} \approx 1.5 \times 10^{54} \text{ s}^{-1}, \quad (1)$$

where $f_{\text{Ly}\alpha, 15 \text{ kpc}} = 2.99 \pm 0.01 \times 10^{-16} \text{ erg s}^{-1} \text{ cm}^{-2}$, corresponding to $L_{\text{Ly}\alpha, 15 \text{ kpc}} = 1.7 \times 10^{43} \text{ erg s}^{-1}$. We have assumed that $\approx 68\%$ of the ionizing photons are converted into Ly α emission (Spitzer 1978). This is a lower limit of Ly α , because it may be destroyed by dust.

Using the same spatial region, we measured that the He II emission has a flux of $f_{\text{He II}} = 7.8 \pm 0.2 \times 10^{-17} \text{ erg s}^{-1}$ ($L_{\text{He II}} = 3.2 \pm 0.1 \times 10^{42} \text{ erg s}^{-1}$). We calculated the He⁺ ionizing photon number ($E_{\nu} \geq 54.4 \text{ eV}$) using the equation

$$Q(\text{He}^+) = \frac{L_{\lambda 1640}}{h\nu_{\lambda 1640}} \frac{\alpha_{\text{He II}}^{\text{eff}}}{\alpha_{\text{He II}}^{1640}} \approx 2.8 \times 10^{53} \text{ s}^{-1}, \quad (2)$$

where we assumed the case B recombination model, with a temperature of $T = 10^4 \text{ K}$. Under this assumption, $\alpha_{\text{He II}}^{\text{eff}}(T) = 1.53 \times 10^{-12} \text{ cm}^3 \text{ s}^{-1}$ (Prescott et al. 2009).

Therefore, $Q(\text{He}^+)/Q(\text{H})$ is equal to 0.19. Note this is an upper limit for the $Q(\text{He}^+)/Q(\text{H})$ ratio because Ly α could be destroyed by dust. The $Q(\text{He}^+)/Q(\text{H})$ ratio suggests that the powering source of MAMMOTH-1 produces a hard ionizing radiation spectrum. In comparison, if we assume a typical Pop II stellar population with a Salpeter IMF and a low metallicity of $Z = 10^{-4} Z_{\odot}$, then $Q(\text{He}^+)/Q(\text{H})$ equals 0.005 (Schaerer 2003; Prescott et al. 2009), two orders of magnitude smaller than the value we estimated from MAMMOTH-1. This hard ionization ratio could arise because of significantly lower metallicity (e.g., Population III), a stellar population with a top-heavy IMF (Schaerer 2003; Tumlinson et al. 2003; Cai et al. 2011), or an AGN. The detection of strong C IV and C III] emission makes this nebula unlikely to be powered by a low-metallicity (e.g., Pop III) stars. Our current data support the conclusion that this ELAN is powered by one or more hard ionizing sources (e.g., AGN).

4.2. Sources of the Enormous Ly α , Strong Extended C IV, and He II Emission in a Radio-quiet System

At least 15 Ly α nebulae with Ly α spatial extents larger than 150 kpc have recently been discovered (e.g., Cantalupo et al. 2014; Hennawi et al. 2015; Borisova et al. 2016). But in none of these nebulae have strongly extended He II and C IV been reported. We will discuss below several mechanisms that may power MAMMOTH-1.

4.2.1. Photoionization Model

In photoionization models, C IV emission is mainly powered by collisional excitation (e.g., Arrigoni Battaia et al. 2015b). The intensity of collisional excitation has a strong dependence on the temperature (e.g., Gurzadyan 1997). A higher ionization parameter (U) yields a higher gas temperature, and thus the C IV intensity strongly depends on the ionization parameter. Collisional excitation also depends on the gas density and column density of C IV. The He II emission is mainly due to recombination. The fraction of He II emission reaches a peak at $U \sim -2.0$, where a larger fraction of the helium has been doubly ionized (e.g., Arrigoni Battaia et al. 2015a). Higher ionization parameters only modestly change the He II intensity. The C III] emission increases with the ionization parameter, and it is also highly sensitive to the metallicity. The C III] emission peaks at a gas metallicity of $Z \sim 0.2 \times Z_{\odot}$, and it decreases at both higher and lower metallicities (Erb et al. 2009). Therefore, the combination of He II, C IV, and C III] strongly constrains the physical properties of the CGM.

Using CLOUDY ionization modeling (Ferland 1996), Arrigoni Battaia et al. (2015b) have thoroughly investigated the He II/Ly α and C IV/Ly α ratios under different ionization parameters, gas densities (n_{H}), and QSO ionizing luminosities ($L_{\nu_{\text{Ly}\alpha}}$) for the Slug nebula and nebulae in the SSA22 protocluster. In Section 3, we suggest that MAMMOTH-1 could be powered mainly by source B. Source B may be a

Table 3
A Comparison between the Ly α Nebula MAMMOTH-1 and Other Enormous Ly α Nebulae

Name	L_{total} (10^{43} erg s $^{-1}$)	L_{nebula} (10^{43} erg s $^{-1}$)	Size ^a (kpc)	Ionizing Sources	$L_{\text{C IV}}/L_{\text{Ly}\alpha}$	$L_{\text{He II}}/L_{\text{Ly}\alpha}$
MAMMOTH-1	52.8 ± 0.1	49.0 ± 1.0	≈ 440	faint source ($U = 25.8, B = 23.7, V = 24.3, i = 24.3$)	0.12 ± 0.01	0.12 ± 0.01
Slug ^b	143.0 ± 5.0	≈ 22.0	≈ 500	ultraluminous QSO	< 0.12 (2σ)	< 0.08 (2σ)
Jackpot ^c	≈ 20.0		≈ 310	QSO quartet, ultraluminous QSO		
Q0042-2627 ^d	17.0		318	ultraluminous QSO	< 0.01 (2σ)	< 0.01 (2σ)
CTS G18.01 ^d	19.0		239	ultraluminous QSO	< 0.04 (2σ)	< 0.03 (2σ)

Notes.

^a We define size for a surface brightness $SB \geq 4.8 \times 10^{-18}$ erg s $^{-1}$ cm $^{-2}$ arcsec $^{-2}$. For the other Ly α nebulae, the luminosities are just cited from the published papers, without defining a surface brightness threshold.

^b The parameters of the Slug nebula are from Cantalupo et al. (2014) and Arrighi-Batta et al. (2015a).

^c The parameters of the Jackpot nebula are from Hennawi et al. (2015).

^d The parameters of the two Ly α nebulae, Q0042-2627 and CTS G18.01, are from the MUSE Ly α nebulae survey (Borisova et al. 2016).

strongly obscured source, for example, a type II AGN. The Ly α emission from a strongly obscured source may be complicated to interpret. In this section, we conduct studies similar to that of Arrighi Battaia et al. (2015b), but we focus on reproducing the He II surface brightness and the C IV/He II and C III]/He II line ratios. In our CLOUDY modeling, the AGN continuum follows the recipe in Mathews & Ferland (1987). We assume that the CGM clouds have a constant hydrogen density (n_{H}). We assume that the emitting gaseous clouds are uniformly distributed throughout the halo, and we further assume a standard plane-parallel geometry for these clouds. To match our measurements in Section 3.3, we assume that the distance between the CGM cloud and the central QSO is $R \approx 15$ kpc. In our CLOUDY models, we try combinations of different n_{H} values, with $n_{\text{H}} = 0.01$ – 10.0 cm $^{-3}$ (steps of 0.5 dex), different ionization parameters, with $\text{Log } U = -3 - 1$ (steps of 0.5 dex), different column densities of $N_{\text{H}} = 10^{19} - 10^{22}$ cm $^{-2}$ (steps of 0.5 dex), and metallicities with $Z = (0.1 - 1.0) \times Z_{\odot}$ (steps of $0.5 \times Z_{\odot}$). We assume a gas covering fraction of $f_{\text{C}} = 0.3$ (e.g., Cantalupo et al. 2014).

Our observed He II surface brightness is $SB_{\text{He II}} \approx 3.3 \times 10^{-17}$ erg s $^{-1}$ cm $^{-2}$ arcsec $^{-2}$. We require that the parameter combinations yield a He II surface brightness of $\approx (3.0 - 3.5) \times 10^{-17}$ erg s $^{-1}$ cm $^{-2}$ arcsec $^{-2}$ to roughly match the observed He II emission. In Figure 7, we present models that yield the observed He II surface brightness, and we present our observed value using a red dot with an error bar. Using the parameter combinations with $(N_{\text{H}}, Z, \text{Log}(U), n_{\text{H}}) = (10^{20}$ cm $^{-2}, 0.5 Z_{\odot}, -2, 0.1$ cm $^{-3})$ and $(10^{18}$ cm $^{-2}, 1.0 Z_{\odot}, -2, 2.0$ cm $^{-3})$ reproduces the observed intensities of He II, C IV, and C III] and the line ratios of C IV/He II and C III]/He II within 1σ errors (red error bars in Figure 7). Therefore, the C IV/He II and C III]/He II line ratios are consistent with AGN photoionization.

4.2.2. Resonant Scatter

In Section 3, we have shown that the Ly α , C IV, and He II emission line profiles contain at least two major components. Double-peaked Ly α emission is predicted by the resonant scattering of Ly α photons (e.g., Dijkstra et al. 2006; Yang et al. 2014). The key prediction of these radiative transfer (RT) calculations is that the Ly α spectrum is double peaked with an enhanced blue peak, producing a blueshift of the Ly α profile. Although it is true that this prediction matches the Ly α profile

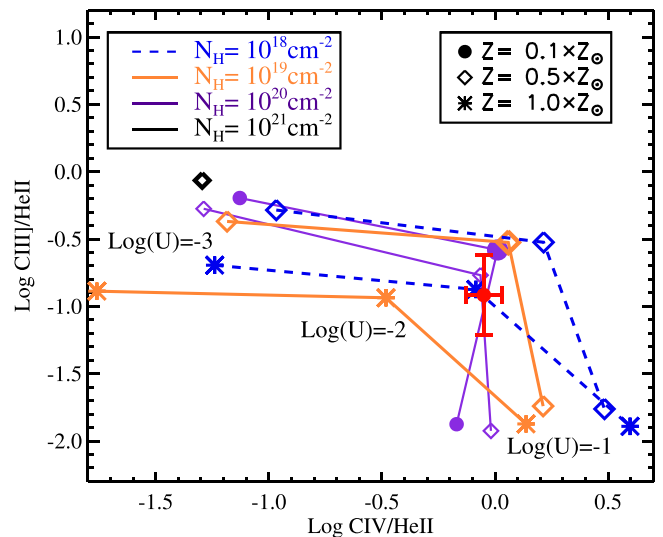


Figure 7. Simulation of the intensity ratios of C IV/He II and C III]/He II powered by AGNs. The colors represent different ionization parameters ($\text{Log } U$), and the symbols represent different metallicities of the gaseous clouds. The observed value is marked with red points with an error bar. MAMMOTH-1 is consistent with the photoionization scenario, with an ionization parameter of $\text{Log } U \approx 2$ and a gas metallicity of $0.1 Z_{\odot}$.

of MAMMOTH-1, the He II emission has the same double-peaked structure as Ly α . He II is an optically thin, nonresonant emission line whose photons escape the halo without RT effects (e.g., Yang et al. 2014). The nonresonant, optically thin emission lines should directly reflect the spatial distribution and kinematics of the gas. Thus, the emission-line structure of He II strongly suggests that the double peaks are due to the actual kinematics (e.g., gas flows) rather than the RT effects.

4.2.3. Shocks due to a Gas Flow

The shocks due to flowing gas can also explain the double peaks of the emission lines. If the fast wind of an outflow is launched, then the shock could heat the surrounding interstellar gas over scales of $\gtrsim 50$ kpc (Debuhr et al. 2012; Harrison et al. 2014). Current galaxy formation simulations and observations suggest that high-velocity ($v_{\text{max}} \sim 1000$ km s $^{-1}$) galactic outflow can quench star formation in the most massive galaxies and eject heavy elements into the IGM (e.g., Taniguchi & Shioya 2000; Martin 2005; Ho et al. 2014). Such galactic

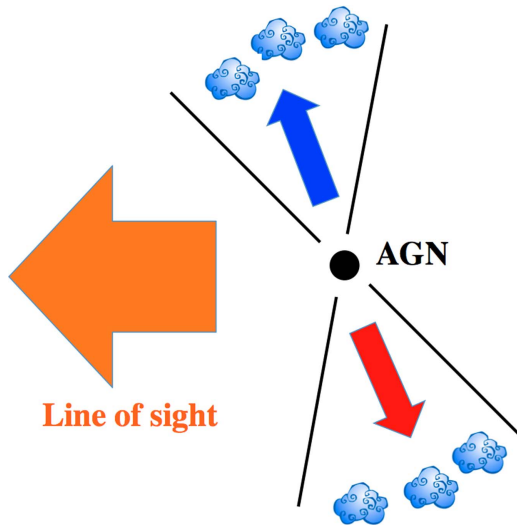


Figure 8. A schematic diagram to demonstrate the outflow interpretation of the data. The C IV and He II velocity offsets between the two components and the spatial extent of emission lines shown in Figure 5 strongly depend on the orientation of the outflow with respect to the line of sight. For a given AGN outflow, if the axis of the outflow is oriented along the line of sight, high-velocity offsets and a small spatial extent would be observed. Conversely, if the axis of the outflow is in the plane of the sky, a small velocity offset and a large spatial extent would be seen.

winds can be driven by (1) intense star formation or (2) relativistic winds or jets resulting from gas accretion onto the SMBHs (e.g., Leitherer et al. 1999; Tombesi et al. 2015).

Wilman et al. (2005) find a Ly α blob at $z = 3.09$ in the SSA22 overdensity (Steidel et al. 2000; Matsuda et al. 2005) whose double-peaked line profile is consistent with a simple outflow model. This model suggests that the Ly α emission is absorbed by a foreground shell of neutral gas that is pushed out up to ≈ 70 kpc by an AGN-driven outflow. Using MAPPINGS (Dopita & Sutherland 1996) and CLOUDY (Ferland 1996) modeling, Villar-Martín et al. (1999, 2007) and Moy & Rocca-Volmerange (2002) suggest both shocks and AGN photoionization could power the extended Ly α , He II, and C IV observed in radio galaxies. Using hydrodynamical simulations, Cabot et al. (2016) further argue that the Ly α , He II, and C IV emission in $z \approx 3$ Ly α blobs could be primarily due to the shocks. Integral field spectrometer (IFS) observations suggest that the high-velocity ($v_{\max} \approx 1000 \text{ km s}^{-1}$) [O III] outflows exist in a sample of five radio-quiet ULIRGs at $z \gtrsim 2$. Such [O III] outflows are consistent with the AGN-driven wind scenario (e.g., Alexander et al. 2010; Harrison et al. 2012).

MAMMOTH-1 has C III]/He II and C IV/He II line ratios consistent with both photoionization and shock models (see Figures 2 and 3 of Villar-Martín et al. 1999). Further, the C IV/Ly α and He II/Ly α ratios of MAMMOTH-1 are consistent with the predictions using shock models (Arrigoni Battaia et al. 2015b), with a gas density $n_{\text{H}} \sim 0.1\text{--}1 \text{ cm}^{-3}$ and a shock velocity of $500\text{--}600 \text{ km s}^{-1}$. If the extended He II and C IV are powered by shocks due to an AGN-driven outflow, then the double velocity peaks of emission lines can be naturally interpreted. Like Harrison et al. (2014), we draw a schematic diagram to illustrate the outflow interpretation of the extended C IV and He II (Figure 8). The velocity offsets between the two components and the spatial extent of emission lines strongly depend on the orientation of the outflow with respect to the line of sight: if the axis of the outflow is oriented

along the line of sight, then a high-velocity offset and a small spatial extent should be observed; conversely, if the axis of the outflow is in the plane of the sky, then a small velocity offset and a large spatial extent should be observed.

From Section 3.2, the offset between two velocity components is $\approx 700 \text{ km s}^{-1}$. These line structures are similar to the ULIRG sample in Harrison et al. (2012). The AGN outflow is a natural explanation of the extended metal-line emission. If we assume the extended C IV and He II are due to the AGN outflow, then we can estimate the energy of the outflow.

To make an order-of-magnitude estimation of the outflow energy, we follow the model proposed by Heckman et al. (1990; also see Nesvadba et al. 2008; Harrison et al. 2012). This model assumes a energy-conserving bubble inflated by AGN outflow expanding into a uniform CGM with a constant density. Further, this model assumes that the outflow injects energy into the CGM at a constant rate. Then, Heckman et al. (1990) derived the following equation to calculate the injected energy coupled to the CGM (E_{kin}):

$$E_{\text{kin}} \approx 1.5 \times 10^{46} r_{10}^2 v_{1000}^3 n_{0.5} \text{ erg s}^{-1}, \quad (3)$$

where v_{1000} is the velocity offset between two components in units of 1000 km s^{-1} , and r_{10} is the radius of the observed C IV emission in units of 10 kpc. The ambient density is the gas density ahead of the expanding bubble, in units of 0.5 cm^{-3} . The total energy injected is $E_{\text{in}} = E_{\text{kin}}/\eta$, where η is the coupling efficiency. The coupling efficiency represents the fraction of the outflow energy that is coupled to the CGM gas. The value of η could range from 0.05 to 0.8 (Nesvadba et al. 2008). For MAMMOTH-1, if we assume that the extended C IV and He II are completely powered by an AGN outflow, and the axis of the outflow is oriented 45° with respect to the sight line, then $r_{10} = 2$ and $v_{1000} = 0.7$. It is actually hard to find a direct way to estimate the electron density $n_{0.5}$. We assume the electron density $n_{0.5} = 1\text{--}4$, which values were indirectly measured from Heckman et al. (1990) and were adopted by Heckman et al. (1990), Nesvadba et al. (2008), and Harrison et al. (2012) when they calculated the AGN feedback energy at $z = 2\text{--}3$. Taking these numbers into Equation (3), we can make an order-of-magnitude estimation that the outflow in MAMMOTH-1 injects energy into the CGM at a considerable rate of $\sim 10^{45\text{--}47} \text{ erg s}^{-1}$. Over a typical AGN duty cycle of 30 Myr (e.g., Hopkins et al. 2005; Harrison et al. 2012), the total energy injected reaches the order of $10^{60\text{--}62} \text{ erg}$. According to Nesvadba et al. (2006), the typical binding energy of a massive elliptical galaxy with a halo mass of $M_{\text{halo}} \approx 10^{12} M_{\odot}$ is about 10^{60} erg . Thus, if MAMMOTH-1 is powered by an AGN outflow, then the outflow energy could be comparable to one or two orders of magnitude higher than this binding energy, making a vast AGN outflow possibly play a major role in heating the ISM.

It has also long been suggested that jet-induced shocks can power extended metal-line emission, and extended C IV emission has been reported in a few radio galaxies with strong radio continua (e.g., McCarthy 1993; Villar-Martín et al. 2007). We argue that our current data disfavor the model of jet-ISM interaction. From the FIRST radio catalog (Becker et al. 1995), we do not find any source with a radio flux at $1.4 \text{ GHz} > 0.9 \mu\text{Jy}$ within a radius of 30 arcsec from

MAMMOTH-1. Assuming a radio spectrum $S(\nu) \propto \nu^{-0.8}$, this 3σ upper limit corresponds to a luminosity density of $<3.2 \times 10^{32} \text{ erg s}^{-1} \text{ Hz}^{-1}$ at rest-frame 1.4 GHz (Yang et al. 2009). This limit is two orders of magnitude lower than the radio continua of other Ly α nebulae powered by radio galaxies (e.g., Carilli et al. 1997; Reuland et al. 2003).

4.2.4. Gravitational Cooling Radiation

Theoretical studies have suggested that Ly α nebula could result from the gravitational cooling radiation (e.g., Haiman & Rees 2001; Dijkstra et al. 2006; Yang et al. 2006; Faucher-Giguère et al. 2010; Rosdahl & Blaizot 2012). Several studies have predicted the He II cooling radiation using hydrodynamical simulations. Yang et al. (2006) predict that the He II line has the FWHM $\leq 400 \text{ km s}^{-1}$ even for the most massive halo at $z \approx 2$ ($M \sim 10^{14} M_{\odot}$). If our observed He II line profile has two major velocity components as shown in Figure 5, then the He II has a large FWHM of $714 \pm 100 \text{ km s}^{-1}$ for the blue component and $909 \pm 130 \text{ km s}^{-1}$ for the red component. The observed FWHMs are much wider than the predicted line width for cooling radiation. Also, using hydrodynamical simulations, Fardal et al. (2001) and Yang et al. (2006) point out that the He II regions should be centrally concentrated, and the He II cooling radiation may be too small to resolve using current ground-based telescopes. This size prediction of the He II cooling radiation does not fit our observations. We have detected extended He II emission over a $\gtrsim 30 \text{ kpc}$ scale. Further, if the Ly α emission results from the cooling inflow of the pristine gas in the intergalactic filaments, then we should expect no extended C IV to be detected (e.g., Yang et al. 2006; Arrigoni Battaia et al. 2015b). Therefore, we conclude that our current observations do not fit with the cooling radiation picture.

5. Summary

In this paper, we present our discovery of an ELAN MAMMOTH-1 at $z = 2.319$ in the density peak of the large-scale structure BOSS1441 (Cai et al. 2016). Above the 2σ surface brightness contour, this object has the highest nebular luminosity discovered to date: $L_{\text{Ly}\alpha} = 5.1 \pm 0.1 \times 10^{44} \text{ erg s}^{-1}$ (excluding the Ly α PSF; see Section 3). Above the 2σ surface brightness limit of $\text{SB}_{\text{Ly}\alpha} = 4.8 \times 10^{-18} \text{ erg s}^{-1} \text{ cm}^{-2} \text{ arcsec}^{-2}$, we measure this nebula to have an end-to-end spatial extent of $\sim 442 \text{ kpc}$, comparable to the largest known Ly α nebula (e.g., Cantalupo et al. 2014).

MAMMOTH-1 is associated with a relatively faint source in the broadband (source B, Figure 1). This source has an extended He II and C IV emission in our LBT/MODS spectra (Figure 5). No radio sources are detected from the FIRST radio catalog (Becker et al. 1995) within $30''$ from the center of MAMMOTH-1 (Section 3). Both C IV and He II have a spatial extent of $\gtrsim 30 \text{ kpc}$. The Ly α , He II, and C IV emissions all contain two major components, with velocity offsets of $\approx 700 \text{ km s}^{-1}$ (Section 4.2). The large spatial extent of the Ly α emission, the extended He II and C IV emission, and the double-peaked line profiles make MAMMOTH-1 unique compared to all of the ELANe discovered to date.

We discussed several explanations for MAMMOTH-1. We consider different scenarios, including photoionization (Section 4.2.1), resonant scattering (Section 4.2.2), shocks due to gas flows (Section 4.2.3), and cooling radiation

(Section 4.2.4). We ruled out resonant scattering and cooling radiation as unlikely. Our current data support photoionization (Figure 8) or shocks due to the galactic outflow as the source of the extended Ly α emission. The outflow model could naturally generate the double-peaked structures of the He II and C IV emission. Future integral field spectroscopy can examine if this ELAN is powered by a group of galaxies and also can help us to better understand the nature of MAMMOTH-1.

Z.C. acknowledges the valuable comments from Fabrizio Arrigoni Battaia, Joe Hennawi, and Arjue Dey. Z.C., X.F., and I.M. thank the support from the US NSF grant AST 11-07682. Z.C. and J.X.P. acknowledge support from NSF AST-1412981. Y.Y.'s research was supported by Basic Science Research Program through the National Research Foundation of Korea (NRF) funded by the Ministry of Science, ICT & Future Planning (NRF 2016R1C1B2007782). A.Z. acknowledges support from NSF grant AST-0908280 and NASA grant ADP-NNX10AD47G. S.C. gratefully acknowledges support from Swiss National Science Foundation grant PP00P2_163824. N.K. acknowledges support from the JSPS grant 15H03645. This work is based on observations at Kitt Peak National Observatory, National Optical Astronomy Observatory (NOAO Prop. ID: 2013A-0434; PI: Z. Cai; NOAO Prop. ID: 2014A-0395; PI: Z. Cai), which is operated by the Association of Universities for Research in Astronomy (AURA) under cooperative agreement with the National Science Foundation. The authors are honored to be permitted to conduct astronomical research on Iolkam Du'ag (Kitt Peak), a mountain with particular significance to the Tohono O'odham. The LBT is an international collaboration among institutions in the United States, Italy, and Germany. The LBT Corporation partners are The University of Arizona on behalf of the Arizona university system; Istituto Nazionale di Astrofisica, Italy; LBT Beteiligungsgesellschaft, Germany, representing the Max Planck Society, the Astrophysical Institute Potsdam, and Heidelberg University; The Ohio State University; and The Research Corporation, on behalf of The University of Notre Dame, University of Minnesota, and University of Virginia.

References

- Adelberger, K. L., Shapley, A. E., Steidel, C. C., et al. 2005, *ApJ*, 629, 636
 Alexander, D. M., Swinbank, A. M., Smail, I., McDermid, R., & Nesvadba, N. P. H. 2010, *MNRAS*, 402, 2211
 Allen, M. G., Groves, B. A., Dopita, M. A., Sutherland, R. S., & Kewley, L. J. 2008, *ApJS*, 178, 20
 Arrigoni Battaia, F., Hennawi, J. F., Prochaska, J. X., & Cantalupo, S. 2015a, *ApJ*, 809, 163
 Arrigoni Battaia, F., Yang, Y., Hennawi, J. F., et al. 2015b, *ApJ*, 804, 26
 Becker, R. H., White, R. L., & Helfand, D. J. 1995, *ApJ*, 450, 559
 Borisova, E., Cantalupo, S., Lilly, S. J., et al. 2016, arXiv:1605.01422
 Bouwens, R. J., Ilingworth, G. D., Oesch, P. A., et al. 2011, *ApJ*, 737, 90
 Byard, P. L., & O'Brien, T. P. 2000, *Proc. SPIE*, 4008, 934
 Cabot, S. H. C., Cen, R., & Zheng, Z. 2016, arXiv:1603.09696
 Cai, Z., Fan, X., Bian, F., et al. 2016, arXiv:1609.02913
 Cai, Z., Fan, X., Jiang, L., et al. 2011, *ApJL*, 736, L28
 Cai, Z., Fan, X., Jiang, L., et al. 2015a, *ApJL*, 799, L19
 Cai, Z., Fan, X., Peirani, S., et al. 2015b, arXiv:1512.06859
 Cantalupo, S., Arrigoni-Battaia, F., Prochaska, J. X., Hennawi, J. F., & Madau, P. 2014, *Natur*, 506, 63
 Cantalupo, S., Porciani, C., Lilly, S. J., & Miniati, F. 2005, *ApJ*, 628, 61
 Carilli, C. L., Röttgering, H. J. A., van Ojik, R., et al. 1997, *ApJS*, 109, 1
 Cen, R., Miralda-Escudé, J., Ostriker, J. P., & Rauch, M. 1994, *ApJL*, 437, L9
 Cen, R., & Ostriker, J. P. 2006, *ApJ*, 650, 560
 Colberg, J. M., Krughoff, K. S., & Connolly, A. J. 2005, *MNRAS*, 359, 272

- Dawson, K. S., Schlegel, D. J., Ahn, C. P., et al. 2013, *AJ*, 145, 10
- Debuhr, J., Quataert, E., & Ma, C.-P. 2012, *MNRAS*, 420, 222
- Dey, A., Bian, C., Soifer, B. T., et al. 2005, *ApJ*, 629, 654
- Dijkstra, M., Haiman, Z., & Spaans, M. 2006, *ApJ*, 649, 14
- Dijkstra, M., & Loeb, A. 2009, *MNRAS*, 400, 1109
- Dopita, M. A., & Sutherland, R. S. 1996, *ApJS*, 102, 161
- Erb, R. M., Son, H. S., Samanta, B., Rotello, V. M., & Yellen, B. B. 2009, *Natur*, 457, 999
- Fardal, M. A., Katz, N., Gardner, J. P., et al. 2001, *ApJ*, 562, 605
- Faucher-Giguère, C.-A., Kereš, D., Dijkstra, M., Hernquist, L., & Zaldarriaga, M. 2010, *ApJ*, 725, 633
- Ferland, G. J. 1996, University of Kentucky Internal Report 565
- Francis, P. J., Williger, G. M., Collins, N. R., et al. 2001, *ApJ*, 554, 1001
- Fumagalli, M., Prochaska, J. X., Kasen, D., et al. 2011, *MNRAS*, 418, 1796
- Fukugita, M., & Peebles, P. J. E. 2004, *ApJ*, 616, 643
- Geach, J. E., Alexander, D. M., Lehmer, B. D., et al. 2009, *ApJ*, 700, 1
- Geach, J. E., Bower, R. G., Alexander, D. M., et al. 2014, *ApJ*, 793, 22
- Geach, J. E., Narayanan, D., Matsuda, Y., et al. 2016, *ApJ*, 832, 37
- Gould, A., & Weinberg, D. H. 1996, *ApJ*, 468, 462
- Gurzadyan, G. A. 1997, The Physics and Dynamics of Planetary Nebulae XVI, Vol. 513 (Berlin: Springer), 179
- Haiman, Z., & Rees, M. J. 2001, *ApJ*, 556, 87
- Harrison, C. M., Alexander, D. M., Mullaney, J. R., & Swinbank, A. M. 2014, *MNRAS*, 441, 3306
- Harrison, C. M., Alexander, D. M., Swinbank, A. M., et al. 2012, *MNRAS*, 426, 1073
- Hayes, M., Scarlata, C., & Siana, B. 2011, *Natur*, 476, 304
- Heckman, T. M., Armus, L., & Miley, G. K. 1990, *ApJS*, 74, 833
- Heckman, T. M., Miley, G. K., Lehnert, M. D., & van Breugel, W. 1991, *ApJ*, 370, 78
- Hennawi, J. F., & Prochaska, J. X. 2013, *ApJ*, 766, 58
- Hennawi, J. F., Prochaska, J. X., Cantalupo, S., & Arrigoni-Battaia, F. 2015, *Sci*, 348, 779
- Hernquist, L., Katz, N., Weinberg, D. H., & Miralda-Escudé, J. 1996, *ApJL*, 457, L51
- Ho, I.-T., Kewley, L. J., Dopita, M. A., et al. 2014, *MNRAS*, 444, 3894
- Hopkins, P. F., Hernquist, L., Cox, T. J., et al. 2005, *ApJ*, 630, 716
- Kollmeier, J. A., Zheng, Z., Davé, R., et al. 2010, *ApJ*, 708, 1048
- Lee, K.-G., Hennawi, J. F., White, M., Croft, R. A. C., & Ozbek, M. 2014, *ApJ*, 788, 49
- Leitherer, C., Schaerer, D., Goldader, J. D., et al. 1999, *ApJS*, 123, 3
- Martin, C. L. 2005, *ApJ*, 621, 227
- Martin, C. L., Shapley, A. E., Coil, A. L., et al. 2012, *ApJ*, 760, 127
- Martin, D. C., Chang, D., Matuszewski, M., et al. 2014, *ApJ*, 786, 107
- Martin, D. C., Matuszewski, M., Morrissey, P., et al. 2015, *Natur*, 524, 192
- Mathews, W. G., & Ferland, G. J. 1987, *ApJ*, 323, 456
- Matsuda, Y., Yamada, T., Hayashino, T., et al. 2005, *ApJL*, 634, L125
- McCarthy, P. J. 1993, *ARA&A*, 31, 639
- Miley, G., & De Breuck, C. 2008, *A&ARv*, 15, 67
- Miralda-Escudé, J., Cen, R., Ostriker, J. P., & Rauch, M. 1996, *ApJ*, 471, 582
- Moy, E., & Rocca-Volmerange, B. 2002, *A&A*, 383, 46
- Mathews, W. G., & Ferland, G. J. 1987, *ApJ*, 323, 456
- Nesvadba, N. P. H., Lehnert, M. D., De Breuck, C., Gilbert, A. M., & van Breugel, W. 2008, *A&A*, 491, 407
- Nesvadba, N. P. H., Lehnert, M. D., Eisenhauer, F., et al. 2006, *ApJ*, 650, 693
- Palunas, P., Teplitz, H. I., Francis, P. J., Williger, G. M., & Woodgate, B. E. 2004, *ApJ*, 602, 545
- Prescott, M. K. M., Dey, A., & Jannuzi, B. T. 2009, *ApJ*, 702, 554
- Prochaska, J. X., Weiner, B., Chen, H.-W., Mulchaey, J., & Cooksey, K. 2011, *ApJ*, 740, 91
- Rauch, M. 1998, *ARA&A*, 36, 267
- Reuland, M., van Breugel, W., Röttgering, H., et al. 2003, *ApJ*, 592, 755
- Rosdahl, J., & Blaizot, J. 2012, *MNRAS*, 423, 344
- Schaerer, D. 2003, *A&A*, 397, 527
- Spitzer, L. 1978, Physical Processes in the Interstellar Medium (New York: Wiley)
- Steidel, C. C., Adelberger, K. L., Shapley, A. E., et al. 2000, *ApJ*, 532, 170
- Taniguchi, Y., & Shioya, Y. 2000, *ApJL*, 532, L13
- Tombesi, F., Meléndez, M., Veilleux, S., et al. 2015, *Natur*, 519, 436
- Tumlinson, J., Shull, J. M., & Venkatesan, A. 2003, *ApJ*, 584, 608
- Tumlinson, J., Thom, C., Werk, J. K., et al. 2011, *Sci*, 334, 948
- van Dokkum, P. G. 2001, *PASP*, 113, 1420
- Villar-Martín, M., Binette, L., & Fosbury, R. A. E. 1999, *A&A*, 346, 7
- Villar-Martín, M., Sánchez, S. F., Humphrey, A., et al. 2007, *MNRAS*, 378, 416
- Villar-Martín, M., Tadhunter, C., Morganti, R., Axon, D., & Koekemoer, A. 1999, *MNRAS*, 307, 24
- Wilman, R. J., Gerssen, J., Bower, R. G., et al. 2005, *Natur*, 436, 227
- Yang, Y., Zabludoff, A., Eisenstein, D., & Davé, R. 2010, *ApJ*, 719, 1654
- Yang, Y., Zabludoff, A., Jahnke, K., & Davé, R. 2014, *ApJ*, 793, 114
- Yang, Y., Zabludoff, A., Tremonti, C., Eisenstein, D., & Davé, R. 2009, *ApJ*, 693, 1579
- Yang, Y., Zabludoff, A. I., Davé, R., et al. 2006, *ApJ*, 640, 539